FUNDAMENTALS & APPLICATIONS

CHEMELECTROCHEM

ANALYSIS & CATALYSIS, BIO & NANO, ENERGY & MORE

Accepted Article

Title: Analysis of the solid electrolyte interphase on hard carbon electrodes in sodium-ion batteries

Authors: M. Carboni, J. Manzi, A.R. Armstrong, J. Billaud, Sergio Brutti, and R. Younesi

To be cited as: *ChemElectroChem* 10.1002/celc.201801621

Link to VoR: http://dx.doi.org/10.1002/celc.201801621

A Journal of

ChemPubSoc Europe

WILEY-VCH

www.chemelectrochem.org

ARTICLE WILEY-VCH

Analysis of the solid electrolyte interphase on hard carbon electrodes in sodium-ion batteries

M.Carboni,[a] J. Manzi,[b] A.R.Armstrong,[c] J. Billaud,[c] S. Brutti, *[b] R.Younesi[a]

Abstract: The composition, morphology and evolution of the solid electrolyte interphase (SEI) formed on hard carbon (HC) electrodes upon cycling in sodium-ion batteries are here investigated. A microporous HC was prepared by pyrolysis of D-(+)-Glucose at 1000°C followed by ball-milling. HC electrodes were galvanostatically cycled at room temperature in sodium-ion half-cells using an aprotic electrolyte of 1 M sodium bis(trifluoromethanesulfonyl)imide dissolved in propylene carbonate with 3 wt% fluoroethylene carbonate additive. The evolution of the electrode/electrolyte interface was studied by impedance spectroscopy upon cycling and ex situ by spectroscopy and microscopy. The irreversible capacity displayed by the HC electrodes in the first galvanostatic cycle is probably due to the accumulation of redox inactive Na_xC phases and the precipitation of a porous, organic-inorganic hybrid SEI layer over the HC electrodes. This passivation film further evolves in morphology and composition upon cycling and stabilizes after approximately 10 galvanostatic cycles at low current rates.

Introduction

Sodium-ion battery chemistry is considered a valuable alternative to Li-ion technology for stationary energy storage from renewable energy sources[1]. The current research activities concerning sodium-ion battery chemistry tackle all aspects of the cell formulation [2], i.e. the positive [3] and the negative [4,5] electrode active materials, binders, separators and electrolytes [1,6].

Focusing on negative electrode compounds, the most promising available options studied worldwide are hard carbons (HCs), titanates and conversion materials [4,5,7]. In particular HCs derived from waste biomasses or natural products are very promising; thanks to the easily scalable synthesis procedures, large reversible capacities and low operating voltages [5,8–10].

[a] M.Carboni, PhD; R.Younesi, PhD
Ångström Advanced Battery Centre, Department of Chemistry-Ångström Laboratory
Uppsala University
Uppsala SE-75121, Sweden
E-mail: marco.carboni@kemi.uu.se reza.younesi@kemi.uu.se
[b] J. Manzi, PhD; Sergio Brutti, PhD (corresponding author)
Dipartimento di Chimica
Università di Roma La Sapienza
P.le Aldo Moro 5, 00185 Roma, Italy
E-mail: manzi.jess@gmail.com; sergio.brutti@uniroma1.it
[c] A.R.Armstrong, PhD; J.M.Billaud, PhD
EaStCHEM, School of Chemistry
University of St Andrews
Fife, KY16 9ST, UK
E-mail: ara@st-andrews.ac.uk; juliette.billaud@psi.ch

HCs consist of crystalline nano-domains of few stacked graphene sheets, all packed together in the so-called “falling card model” [11]. The primary polycrystalline particles have extended meso-to-micro porosities with restricted pore-openings: the resulting overall surface area can range from few tens to hundreds of square meters per gram of material depending on the original carbon source, the pyrolysis temperature, the pre and post pyrolysis chemical and mechano-chemical treatments [5]. The most relevant drawbacks of HC negative electrodes in sodium-ion batteries are the irreversible capacity in the first electrochemical Na incorporation/de-incorporation and the unsatisfactory Coulombic efficiencies upon cycling at low current densities [8,12]. These negative performance features originate from the parasitic chemistry due to the degradation of the typical carbonate-based electrolytes at low electrode potentials [6,13].

Generally speaking, organic carbonate-based electrolytes are expected to decompose at potentials smaller than 0.8-0.7 V vs. Li or 0.5-0.4 V vs. Na [6,14], due to electrochemical reduction of the C=O group and the release of small volatile hydrocarbons [15,16]. This degradation, which has been widely explored in lithium cells [14,17], also occurs on HC electrodes in Na batteries driving the formation of a solid electrolyte interphase (SEI). The formation of a stable SEI mitigates further parasitic reactions and allows a reversible electrochemical cycling [6,13,18]. However, the natural precipitation of a compact, stable and suitable passivation film depends on the complex interplay of many concurrent factors, the most relevant ones being: (a) the surface chemistry of the HC and its morphology; (b) the composition of the electrolyte (specific organic carbonate mixture, concentration and nature of the sodium salt), the use of electrolyte additives (e.g. vinyl carbonate, fluoro-ethylene carbonate) and (c) the electrochemical procedure adopted (e.g. galvanostatic current rates, electrode potential cutoffs, potentiostatic holds) [18–20]. Therefore, each HC/electrolyte combination is a unique playground that needs to be specifically addressed and investigated in order to describe its peculiar surface chemistry and SEI formation also exploiting computational analyses using extensive multiscale modeling [21-24].

In this study, we investigate the SEI formation and consolidation on an HC material upon galvanostatic cycling (GC) in a sodium battery using an aprotic electrolyte composed of 1 M sodium bis(trifluoromethanesulfonyl)imide (NaTFSI) dissolved in propylene carbonate (PC) with 3 wt% fluoroethylene carbonate (FEC) additive. The HC has been obtained by the pyrolysis at 1000°C of a simple carbohydrate molecule (i.e. D-(+)-Glucose) followed by a mechanochemical treatment [5,10,23]. The use of NaTFSI as sodium salt in aprotic electrolytes for Na-cells has been proposed by Xia et al. [25] to replace the most commonly used $NaClO_4$ [26] and $NaPF_6$ [27] salts. Since $NaClO_4$ salt is impractical in real applications for safety reasons [20,28], the use of NaTFSI may disclose unique improvements compared to

$NaPF_6$ thanks to its higher thermal stability [29] and the strongly mitigated F^--release due to hydrolysis with water molecules [30]. The FEC additive has been previously reported to enhance the galvanostatic reversibility and the stability of the SEI layer grown on HCs [21,27].

The "Results and Discussion" section is organized as follows: the first sub-section is dedicated to the preliminary HC sample characterization by X-ray diffraction (XRD), Raman spectroscopy, N_2 adsorption (BET) and scanning electron microscopy (SEM). The electrochemical activity of the HC electrodes is Na-cells is presented in the second sub-section, whereas the characterization of the precipitation/evolution of the SEI layer upon cycling is presented in the final three subsections where impedance spectroscopy data (EIS) as well as the ex situ analysis of the electrodes by transmission electron microscopy (TEM), infrared (FTIR) and photoelectron spectroscopy (XPS) are discussed.

Results and Discussion

Preliminary HC characterization. The preliminary physico-chemical characterizations of the HC material obtained after the high temperature annealing are summarized in figure 1.

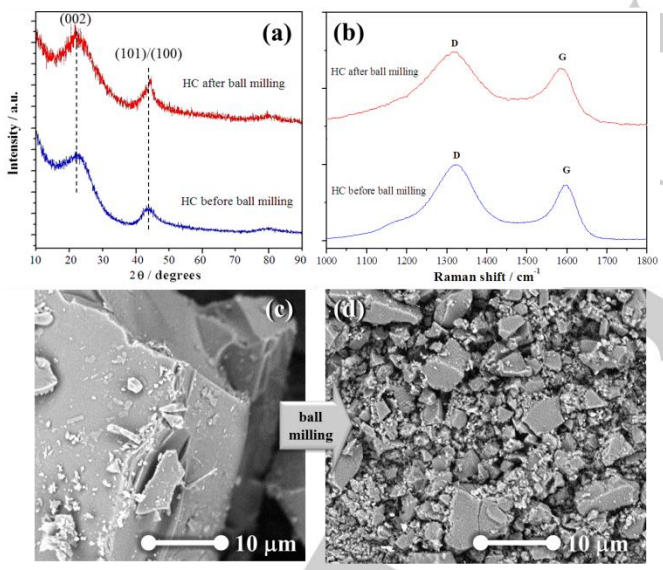

Figure 1. (a) XRD patterns, (b) Raman spectra and (c-d) SEM micrographs of the hard carbon samples before and after ball milling..

The XRD patterns of the HC before and after ball milling show the expected broad peaks in the CuKα 2Θ range 20-25° and 40-45° due to the scattering of the (002) and (101)/(100) lattice planes [5]. The lateral size of the graphene sheets (La) and the stacking height (L_c) can be estimated by the width of these (002) and (101)/(100) diffraction peaks [32]. Apparently, the ball milling slightly increases the L_c value from 1.4±0.2 to 1.6±0.1 nm as well as the La extent from 2.2±0.2 to 2.4±0.1 nm. By considering the d(002) = 3.55 Å distance between the graphene sheets, which is almost unaltered after ball milling, it is possible to estimate the mean number of stacked graphene layers (N_c) [32,33] in both HCs; Nc increases after milling by about 20% from 3.8 to 4.6. These values are in line with the expected crystallite size and shapes reported previously in the literature for pyrolytic carbons [5,32–34].

The Raman spectra of the HC, before and after ball milling show the two expected bands at about 1350 and 1600 cm-1 due to the D-band (E_{2g} graphitic mode) and G-band (defect-induced mode) [35]. The intensity ratio between these two bands, i.e. ID/IG, decreases from 1.5 to 1.2 after ball milling. This is an indication of the enhanced relative ordering of the polycrystalline HC [5] induced by the ball milling, in line with XRD and the literature [32].

The SEM micrographs of the HC before and after ball milling are shown in figure 1c: as expected, the mechanochemical treatment strongly reduces the primary particle size. The expected pulverization of the HC particulate occurs in parallel with an increase in the BET surface area from 720 ± 60 to 1130 ± 150 $m^2 g^{-1.}$ This evidence confirms the expected presence of a large number of micropores with size smaller than a few nanometers [5,12].

Overall the preliminary analysis of the synthesized HC material suggests the formation and the retention after ball milling of the expected "falling card structural motif" [11] where platelet-like crystallites, constituted by a stack of few/small graphene sheets, are randomly packed, thus leaving a large amount of empty voids (micropores) within the primary polycrystalline particles [5].

Electrochemical activity of the HC electrodes in Na-cells. Main The electrochemical activity of the HC material in Na-cells is shown in figure 2. The potential profile at 20 mAg^{-1} (~C/19) shows the expected behaviour for Na-incorporation into HCs: upon discharge, a sloping decrease of the potential is observed from OCV down to approximately 200 mV vs. Na^+/Na (all potential values are hereafter reported vs. Na^+/Na), followed by a pseudo-plateau at approximately 100 mV. The reverse evolution is observed on charge. This behavior originates from the two consecutive sodium incorporation mechanisms in HC, i.e. the insertion within the graphene layers above 200 mV and the ion-electron couple absorption within the microporosity below 200 mV [5,23]. In the first Na-incorporation at 20 mAg^{-1} the HC electrode exhibits 79% of the capacity (i.e. ~450 $mAhg^{-1}$) in the first slope above 200 mV and the remaining 21% (i.e. ~120 $mAhg^{-1}$) in the pseudo plateau at 100 mV (ratio I/A = 4, I = specific capacity delivered above 200 mV, A = specific capacity below 200 mV). The I/A ratio decreases to 2.3 on the first Na extraction where approximately 29% of the capacity is observed below 200 mV and 71% above, and then remains constant in the subsequent galvanostatic cycles. This ratio is larger compared to the available value (I/A = 1) from a similar hard carbon obtained from the pyrolysis of D-(+)-Glucose at 1000°C [23]. This difference possibly originates from the different pyrolysis conditions of the two HCs that may have a remarkable impact on the graphitization/micro-porosity.

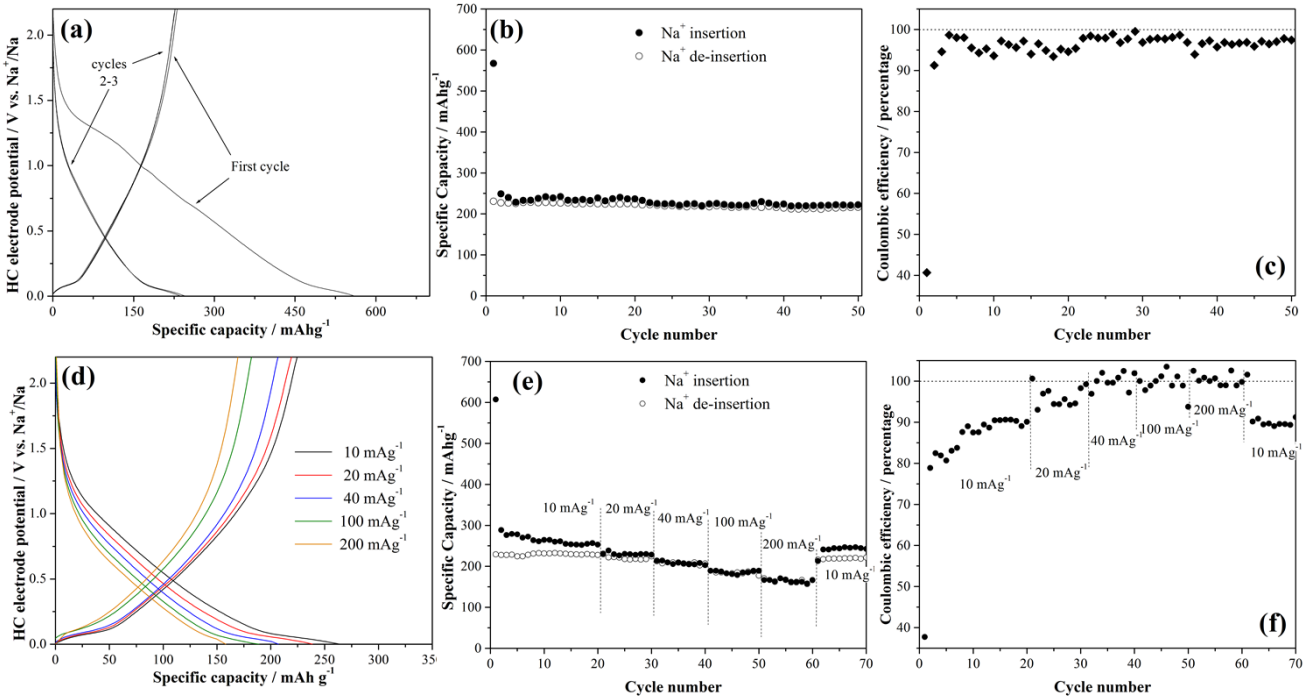

Figure 2. Electrochemical performance of HC in Na half-cells. (a) Evolution of the voltage profile in the firsts 5 galvanostatic cycles at 20 mAg^{-1}; (b) discharge capacity vs. number of cycles and (c) Coulombic efficiency of the HC electrode in a sodium cell at 20 mAg^{-1}; (d) comparison among the voltage profiles recorded at different current rate; (e) rate performance and (f) Coulombic efficiencies of the HC electrode in Na half-cells using 1 M NaTFSI + 3 wt% FEC in PC electrolyte.

The HC shows a large irreversible capacity on the first galvanostatic cycle, 348 mAh g^{-1}, resulting in final Coulombic efficiency (CE) of 41%. This value compares well with values reported by Prabakar et al. [36] (41-44%) from nanoporous hard carbons obtained from the pyrolysis of sucrose, or by Hong et al. [37] (27-54%) from a microporous carbon with a surface area of 1272 m^2 g^{-1}. The irreversible capacity loss is due to the decomposition of the electrolyte and the precipitation of the SEI layer on HC particles, and it is well-known that its extent correlates with the surface area of HC [5].

From the second cycle, the reversible capacity stabilizes at about 220-230 mAh g^{-1} (see figure 2b) and CE above 95% (96.7% mean CE between cycle 40th and 50th). These performances are in line with the available literature on HCs using various electrolytes [5,9,23,25].

Turning to the rate performance shown in figures 2d-e-f, our HC shows a remarkable capacity retention from 10 mAg^{-1} to 200 mAg^{-1} (corresponding to ~C/37 and ~C/2), with measured mean reversible capacities ~230 and ~170 $mAhg^{-1}$, respectively, with a mean working potential in charge (de-sodiation) increasing by 12% from 0.42 to 0.47 V, respectively. It is interesting to observe that the balance between the Na^+ insertion/absorption mechanisms modifies monotonically while increasing the current rate. In fact the analysis of the voltage profiles shown in figure 2d highlights the modification of the I/A ratio from 2.4 ± 0.1 to 2.5 ± 0.1, 2.6 ± 0.2, 2.9 ± 0.1 and 3.3 ± 0.2, for the GC at 10, 20, 40 , 100 and 200 mAg^{-1}, respectively. On the other hand, the CEs at small current rates are unsatisfactory (the mean values of the CE measured at 10 mAg^{-1} and 20 mAg^{-1} being ~90 and CE~97%, respectively). However, at the current rates above 40 mAg^{-1} the CE values approach 100%.

In summary, the performance in Na-cells of the HC electrodes are in line with the available literature both in terms of irreversible capacity loss in the first cycle and reversible specific capacity upon cycling. Moreover a remarkable decrease of the coulombic efficiency upon cycling is observed for current rates as small as 10 mAg^{-1} thus suggesting a notable degradation of the electrolyte at small current rates.

Analysis of the SEI layer evolution: EIS. The evolution of the EIS response upon galvanostatic cycling at 15 mAg^{-1} recorded on the HC electrodes in the charged state (after a complete electrochemical Na de-insertion) is shown in figure 3a. The EIS spectrum comprises two semi-circles, one in the high frequency range (from 100 to 5 kHz) and a second in the mid frequency range (from 1 kHz to 10 Hz), and a linear slope in the low frequency range (frequency < 10 Hz). In consideration of the time constants associated with these three spectral features, one may easily identify the impedance responses of (a) the passivation film grown onto the HC electrodes (high frequency range), (b) the faradaic Na-incorporation process in the HC (mid frequency range) and (c) the electrode pseudo-capacitance in the low frequency range possibly overlapped with sodium solid state diffusion into the HC [19,38–40].

From a qualitative point of view, it is interesting to observe that upon cycling, all these spectral features are always present. However, changes in the size of the semi-circles suggest morphological/composition modification of the interfaces/interphases. The CE value measured at cycle 10

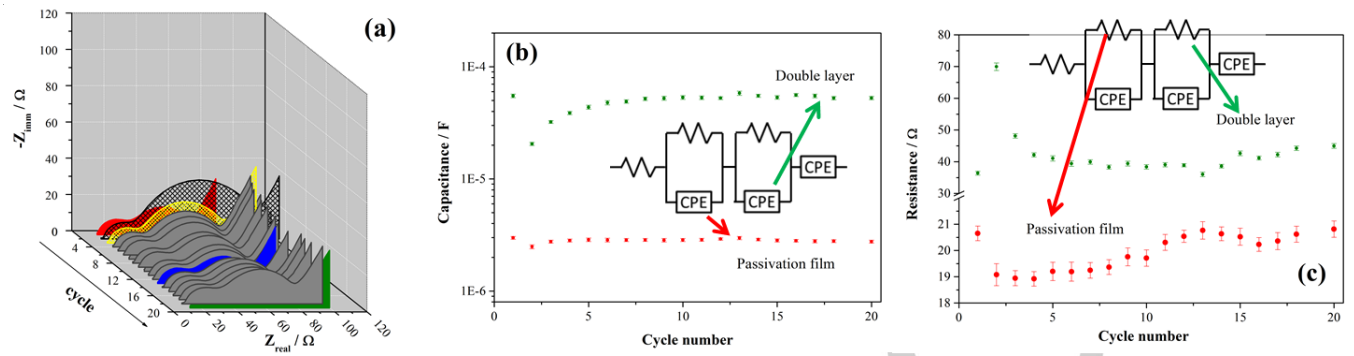

Figure 3. (a) EIS spectra upon cycling (charge / de-sodiated state); evolution of (b) the capacitances (double layer and passivation film) and (c) the resistances (charge transfer and passivation films) upon cycling.

during the EIS experiment is ≈96%, a value very close to the 97% recorded at 20 mA g^{-1}, and much larger compared to the 90% value at 10 mA g^{-1}. It is likely that at 10 mA $g^{-1}$the SEI layer instability increases remarkably: this trend is expected and in line with the available literature of carbonaceous negative electrodes in Na cells [8,12]. In this consideration the EIS spectra confirm the occurrence of parasitic interfacial reactions that modify the overall electrode impedance upon cycling [32,33,41]. Both experiments also suggest that these detrimental processes extend well beyond the first galvanostatic Na incorporation/de-incorporation reactions.

The impedance spectra can be fitted by using an $R_{el}(R_{pf}Q_{pf})(R_{ct}Q_{dl})Q_{cap}$ equivalent circuit, where R_{el}, R_{pf} and R_{ct} represent the electrolyte, passivation film and charge transfer resistances and Q_{pf}, Q_{dl} and Q_{cap} symbolize the passivation film, double layer and pseudo-capacitive capacitances (all capacitances have been fitted with a constant phase element in order to account for possible deviation from ideal capacitive behavior). The evolution of the equivalent circuit fitting parameters is shown in the figures 3b and 3c.

A remarkable modification of the passivation film resistance is observed in the first 1-4 cycles where R_{pf} decreases by approximately 8%. In the following cycles the passivation film resistance increases almost monotonically until cycle 13 and then remains almost constant with limited oscillations. The passivation film capacitance is almost constant upon cycling.

Also, the charge transfer resistance changes considerably in the first few galvanostatic cycles: R_{ct} doubles from the 1st to the 2nd cycle and then decreases by about 45% from cycle 2 to cycle 4. After cycle 5, R_{ct} remains almost constant with a small increasing trend upon cycling (ΔR_{ct}< 0.33 Ω $cycle^{-1}$). This evolution occurs in parallel with the variation of the Q_{dl} that decreases 4 fold between cycle 1 and 2 and then recovers the starting capacitance reaching a stable value from cycle 10.

The EIS spectra analysis confirms the occurrence of physico-chemical alterations of the electrode/electrolyte interface upon cycling. Focusing on the passivation film, the SEI forms during the first Na incorporation/de-incorporation cycle. However, this layer is not stable and its resistance undergoes two opposing effects trends cycle-by-cycle. A possible interpretation of the SEI capacitance/resistance evolutions upon cycling may imply:

(a) a passivation film consolidation from cycle 2 to cycle 4 consisting of a composition modification (i.e. reduction of the film resistance possibly induced by a reduction of the inorganic components) that has no impact on the porosity and thickness of the SEI (i.e. constant capacitance);

(b) a reverse process from cycle 5 to cycle 13 where the passivation layer composition further evolves (i.e. increase of the film resistance possibly driven by the increase of the inorganic constituents), also in this case with a negligible impact on the porosity and thickness of the SEI (i.e. constant capacitance).

Overall the surface chemistry over the HC electrode in a sodium cell is complex and the passivation film formation and stabilization extends to the first 10 galvanostatic cycles at 15 mAg^{-1}.

Analysis of the SEI layer evolution: FTIR and TEM. The evolution of the HC electrode morphology upon cycling has been studied by ex situ TEM on materials recovered from Na cells in the charge state (de-sodiated) after discharge/charge galvanostatic cycles at 15 mAg^{-1} as shown in the figures 4a-f.

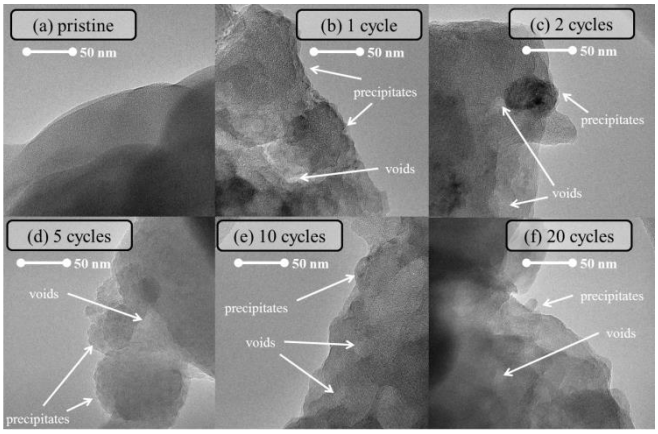

Figure 4. Transmission electron micrographs of the HC electrodes (a) before cycling and (c-f) collected after cycling (de sodiated state).

The surface of the pristine HC is smooth and continuous without remarkable voids or edges. After 1 full GC cycle, a rough and porous SEI layer covers the entire HC surface. Nanometric precipitates with amorphous-like shape/contrast accumulate inhomogeneously over the HC material, leaving voids and fractures. This complex morphology is also observed on samples recovered after 2 or 5 cycles. The most relevant difference between samples recovered after 1 and 5 galvanostatic cycles is an increase of the size of the precipitates and the more homogeneous coverage of the HC surface.

The morphology of the samples recovered after 10 cycles is partially different compared to samples after 5 cycles. A more homogeneous and smooth film covers the surface of the HC: large nanometric amorphous particles are packed together thus forming a composite and porous film with few fractures. Also, in this case many voids/pores are present throughout the film (e.g. area with light contrast). After 20 cycles the morphology is similar with 10-50 nm thick amorphous-like particles accumulated over the surface of the HC leaving 10-20 nm large voids/pores.

The chemical nature of the constituents of the SEI layer grown on the HC particles upon cycling has been studied by ex situ FTIR-ATR spectroscopy as shown in figure 5.

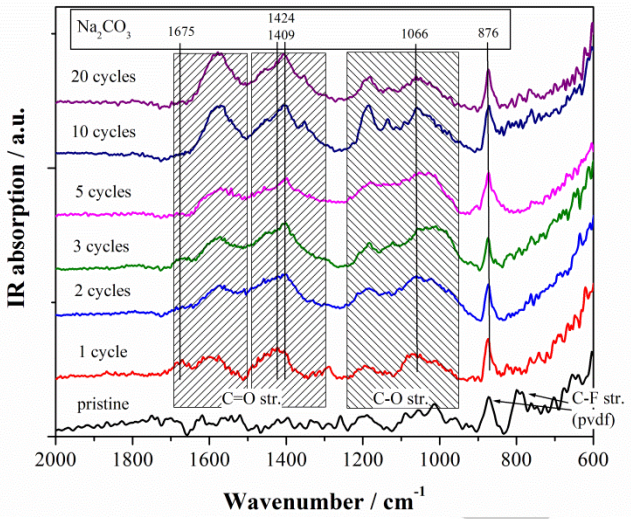

Figure 5. Evolution of the FTIR spectra of the HC electrodes upon cycling.

In all samples recovered after cycling, a typical vibrational fingerprint of organic solid carbonates is present. In fact, all the FTIR-ATR spectra show broad absorption bands in the 1700-1510, 1490-1300, 1250-950 cm^{-1} regions, corresponding to the asymmetric/symmetric stretching of the C=O bond and the stretching of the O-C-O and C-O bonds [14]. These bands possibly overlap/cover the spectral features of the inorganic Na_2CO_3, that shows strong absorptions at 1424, 1409, 876 cm^{-1} and less intense peaks at 1675 and 1066 cm^{-1} [42]. This picture is in line with the previous observations by Guan et al. [43] and by Pan et al. [44], that suggest the formation of an organic carbonate-based SEI layer over the surface of HC, In particular Pan et al. [44] possibly identified the formation of sodium ethylene dicarbonate (SEDC) as the major constituent of the SEI layer grown on an HC cycled in a sodium cell using an EC:DEC (1:2) $NaPF_6$ electrolyte. In our case the formation of SEDC cannot be excluded since all absorption lines of this compound (i.e. 1650, 1305 and 1080 cm^{-1} with strong intensity, 1395 and 820 cm-1 with medium intensity) fall within the broad bands observed for all the cycled HC materials. However, in our case the SEDC compound is not the major constituent of the SEI layer due to the limited intensity of any spectral feature at 1650 cm^{-1} where the most intense absorption of SEDC is expected to occur. This difference is probably due to the different electrolyte used in this study (PC NaTFSI + 3% FEC).

The FTIR-ATR spectra show some evolution of the relative intensity of the broad vibrational bands with increasing cycle number. Overall the absorption peaks become more defined and less broad, thus suggesting a less heterogeneous composition. In particular, the spectral features at 1066 and 1420 cm^{-1} increase in intensity upon cycling. This may suggest the possible increased content of Na_2CO_3 in the samples after 20 cycles compared to HC recovered after few galvanostatic cycles.

In summary the TEM and FTIR ex situ analyses of the electrodes surface confirm the precipitation of the SEI layer over the HC and its evolution upon cycling possibly due to alteration of the inorganic/organic component ratio.

Analysis of the SEI layer evolution: XPS. The chemical composition and evolution of the SEI have been studied by collecting de-sodiated HC electrodes after 1, 2, 3, 5, 10 and 20 discharge/charge galvanostatic cycles at 20 mAg^{-1} and analyzing them by XPS measurements. These spectra were compared with the XP spectrum of the pristine HC electrode and results are shown in Figures 6, 7 and 8 for C 1s, F 1s and O 1s regions, respectively. On passing it is important to underline that the FTIR samples discussed above have been prepared at 15 mA g^{-1} (≈C/25) in agreement with the EIS data. Unfortunately the XPS samples have been prepared at a slightly different current rate (20 mA g^{-1} ≈C/19). Being the corresponding coulombic efficiencies upon cycling very similar (96% and 97% after 10 galvanostatic cycles for C/25 and C/19, respectively) we concluded that the SEI properties are almost identical.

Figure 6a shows the pristine HC electrode before any electrochemical operation. This spectrum was recorded to simplify the interpretation of the XPS signals of the cycled samples. Here, the main component at 284.6 eV is attributed to C–C sp^2 [45–48] of the well-ordered graphite sheets while the peaks at 285.2, 287.5 and 290.1 eV are ascribable to possible surface oxidation and/or defect formation (aliphatic, carbonyl/carboxylic and carbonate groups, respectively) [49–52] probably due to the cracking of the large carbonaceous domains produced by the ball milling process. Two further components at 286.4 (dark green) and at 290.1 eV are assigned to CH_2–CF_2 and to CF_2–CH_2 and, during the curve fitting, the areal ratio between them has been kept equal to 1, according to the symmetrical alternation of CH_2 and CF_2 groups in the chemical structure of the Kynar [53]. A barely visible component at 292.4

eV is associated with the CF_3 groups at the end of the chains of the binder and/or with the CF_3 of TFSI– anion [54,55].

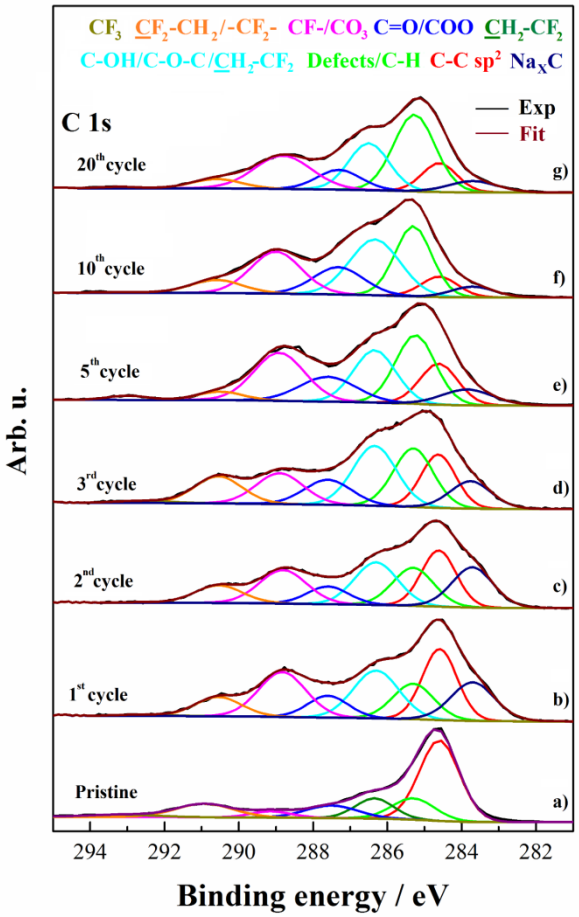

Figure 6. XP spectra of C 1s region for a) pristine HC and HC electrodes after b) 1 cycle, c) 2 cycle, d) 3 cycles, e) 5 cycles, f) 10 cycles and g) 20 cycles.

Figure 6b-g shows the effects of galvanostatic cycling on the surface of HC electrodes up to 20 full cycles. Comparing them with the pristine HC, in these spectra only a new component appears at 283.6-283.9 eV. Along the same lines as reported by several authors for Li-ion batteries, this peak is interpreted as the residual intercalated Na ions into the graphitic framework (NaxC) of the HC [56,57]. Another difference from the pristine HC is that the peak at 286.3-286.4 eV (cyan), previously assigned to CH_2–CF_2 (dark green), is now attributed to alcohol/ether/epoxy [58–60] groups and its area was free to vary during the curve fittings. The contribution of CH_2–CF2 to this peak is challenging to quantify due to the increment of the –CF_2– signals caused by the decomposition of fluorinated species (i.e. FEC and NaTFSI).
After 1 cycle (Figure 6b) the SEI formation and its contribution to the XPS signal is clearly visible. The main component is still the C–C sp^2 but all the other peaks are now enhanced and NaxC signal appears. This suggests that SEI is composed of only a few atomic layers and it is formed by a mixture of organic/inorganic species deriving from the decomposition of solvent, Na salt and FEC. In particular, carbonates (290.1 eV), carboxylates and carbonyl species (287.6 eV) and ethers/epoxides (286.4 eV) are the dominant chemical compounds forming the SEI. Further, the significant presence of aliphatic C–H groups (285.2 eV) can be justified by the unavoidable presence of defects in the graphitic domains. In fact, several authors suggest that a peak at 285.3 eV can also originate from sp^3 or partially sp^2/sp^3 hybridized C sites [49,61].
Beyond the SEI composition, a large quantity of intercalated Na ions (peak at 283.8 eV) are detected in a de-sodiated state. This may explain the reduction of the I/A ratio illustrated in paragraph 3.2. In fact, the contribution to the overall capacity of the electrochemical reactions that happen above 200 mV (i.e. insertion of Na ions into graphene layers) is reduced from 79% to 71% from the first discharge to the first charge. It means that part of the total quantity of Na ions involved in the electrochemical reactions are irreversibly intercalated into the graphitic sheets.
Analyzing the areal ratio of C–C sp^2/Na_xC upon cycling (Figure 6b-g) one may note that this value is 1.45 for the first cycle and it is almost constant during the following cycles (1.35, 1.63, 1.92, 1.76, and 1.81 after 2, 3, 5, 10 and 20 cycles, respectively). Further, the contribution of the sum of their intensities (i.e. $I_{C-C\ sp2}+I_{NaxC}$) to the total intensity of XPS C 1s signal decreases from 35% after the first cycle to 16% after 20 cycles. These considerations imply that a) the amount of sodium trapped in the carbonaceous matrix is almost constant upon cycling, providing a CE close to 100% upon cycling (see paragraph 3.2), b) Na_xC is forming in the inner layers of the electrode and c) the thickness of SEI increases cycle by cycle and it does not involve NaxC compounds.
Similar considerations can be made for the recovered electrodes after 2, 3 and 5 galvanostatic cycles (Figure 6c-e). In these spectra the C–C sp^2 peak, together with its Na_xC shoulder, is still dominant or well detected but reduces its intensity upon cycling. However, the relative enhancement of the defects/C–H, C=O/COO and CO_3/–CF– signals prove the chemical evolution of the SEI and its growth in term of thickness.
The last two samples concern electrodes after 10 and 20 cycles and the XPS results are shown in Figure 6f and 6g, respectively. No significant differences appear between these two spectra: C–C sp^2 peaks with their Na_xC shoulders are now slightly visible while defects/C–H components with the signals of carbon oxidations are predominant. This result underlines that the SEI formation occurs mainly during the first galvanostatic cycle and its chemical composition evolves until the 4th-5th cycle. After that, it becomes stable during subsequent cycles, showing no variations in the spectral profiles after 10 and 20 cycles. Apparently, only the thickness of the interface seems to increase, as already proved by EIS and TEM results.
Turning to the F 1s XP region (Figure 7), in the pristine spectrum (Figure 7a) only one predominant component at 688.1 eV is detected. This signal is related to the –CF_2– group and it is assigned to the fluorinated backbone of the binder [62]. Upon cycling (Figure 7b-7g) this peak broadens due to the –CF_3 groups of the residual NaTFSI (688.8 eV) salt [63], even if the

samples were thoroughly washed with DMC/THF before measuring, and its relative intensity decreases. In parallel a strong component around 284.0 eV appears due to the precipitation of inorganic fluorides [14,49]. This SEI component likely originates from the decomposition of the FEC additive, being the C-F bond more polarized and weak compared to in the trifluoromethyl groups in the $TFSI^-$ anion. [21,26,27,64] The intensity of the component assigned to NaF grows in the first 5 cycles and then stabilizes.

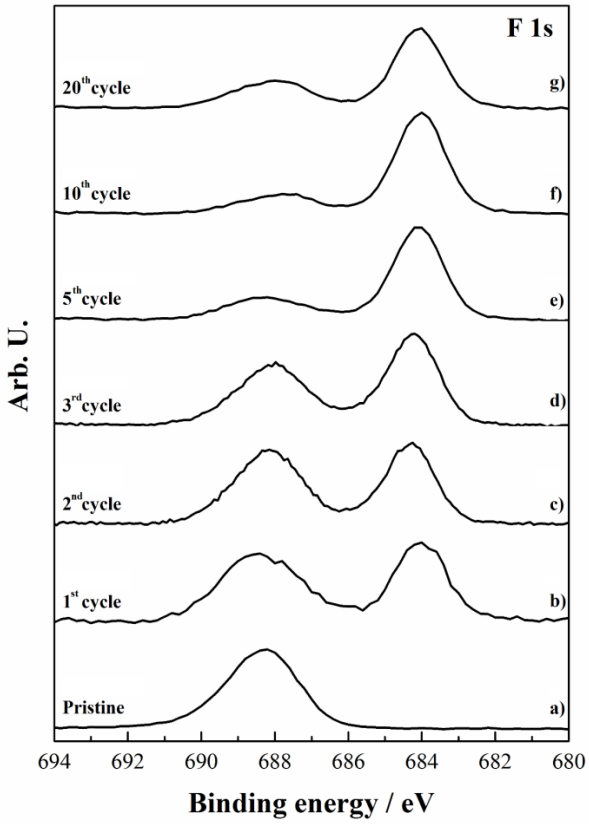

Figure 7. XP spectra of F 1s region for a) pristine HC and HC electrodes after b) 1 cycle, c) 2 cycle, d) 3 cycles, e) 5 cycles, f) 10 cycles and g) 20 cycles..

The evolution of O 1s spectra is shown in figure 8.
As for the F 1s region, only a qualitative analysis is outlined. The surface of the pristine electrode (Figure 8a) shows the typical broad peak (around 532-533 eV) related to adventitious oxygen compounds (i.e. organic C–O and C=O)[49,65]. After cycling (Figure 8b-8g) this feature is still present but the main peak shifts to around 531.0 eV possibly due to the presence of metal carbonates[65] like Na_2CO_3, in agreement with the findings of the FTIR investigation. In passing it may be interesting to observe that the presence of sodiated species on the electrode surfaces is confirmed by the broad band at 536.0 eV due to the Auger Na KLL signal [65,66].
In summary the ex situ XPS analysis of electrodes recuperated after cycling highlights the occurrence of an irreversible Na-trapping in the HC electrodes likely responsible for the large irreversible capacity losses. Moreover the alteration of the C 1s and F 1s XP regions upon cycling confirms and details more clearly the findings of the FTIR study. An hybrid organic/inorganic SEI layer precipitate over the surface of the HC and its composition evolves upon cycling, in particular increasing the NaF content.

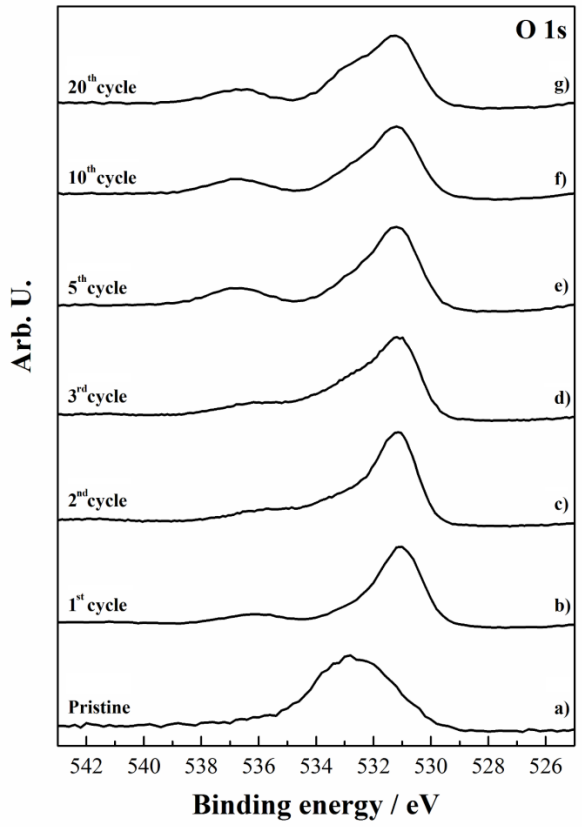

Figure 8. XP spectra of O 1s region for a) pristine HC and HC electrodes after b) 1 cycle, c) 2 cycle, d) 3 cycles, e) 5 cycles, f) 10 cycles and g) 20 cycles

Conclusions

In this study we addressed the SEI formation and consolidation in a sodium battery on HC negative electrode. The large irreversible capacity observed in the first galvanostatic cycle of HC originates from the irreversible trapping of Na+ ions in NaxC compounds as observed by XPS and the precipitation of a porous, organic-inorganic hybrid SEI as highlighted by EIS/FTIR/TEM and XPS. This surface layer precipitates over the HC particles in the first galvanostatic cycle and further evolves in morphology and composition in the following cycles. It is mainly constituted of organic carbonates, Na_2CO_3 and NaF. The SEI layer physico-chemical features stabilize after approximately 5-10 galvanostatic cycles at low current rates thanks to the enrichment in inert inorganic components, Na_2CO_3 and NaF.

Table 1. Binding Energy Positions (BE), Full Widths at Half Maximum (FWHM) values and Gaussian/Lorentzial (G/L) ratio for the pseudo-Voigt functions adopted for the curve fittings.

	BE position (eV)	FWHM (eV)	G/L ratio
Na_xC	283.6-284.9	1.4-2.0	0.9
–C–C– sp^2	284.6-284.7	1.2-1.5	0.8
Defects / –C–H	285.2-285.3	1.2-1.7	0.8
$–\underline{C}H_2–CF_2–$ / C–OH, C–O–C	286.3-286.4	1.2-1.7	0.8
–C=O, COO	287.5-287.6	1.2-1.7	0.8
–CF– / CO_3	288.8-290.2	1.2-1.7	0.8
$–CF_2–CH_2–$ / $–CF_2–$	290.6-290.8	1.2-1.7	0.8
$–CF_3$	292.5-292.7	1.6-2.0	0.9

Experimental Section

HC synthesis. HC material was prepared from an organic precursor, i.e. D-(+)-Glucose (powder, Sigma Aldrich 99.5% purity). D-(+)-Glucose was de-watered (i.e. caramelized) in air at 185 °C for 22 h in an open vessel. The de-watered organic precursor was then pyrolysed in a tubular furnace under a continuous Ar/H_2 flow (4% H_2, 40 ml min^{-1}) following a carefully optimized thermal procedure. The precursor was heated from ambient temperature to 1000 °C with a rate of 1°Cmin-1 and then annealed for 6 hours; the cooling rate was controlled to 10°C min-1. After thermal treatment, the HC was hand ground in an agate mortar and then transferred to a stainless steel jar and mechanochemically ground using two stainless balls (ball to sample weight ratio 10:1, ball diameter 5 mm). The mixer mill was operated for 30 minutes at 900 rpm: the final sample consisted of a black homogeneous powder.

Characterization methods. XRD measurements were carried out using a Phillips Xpert Pro Diffractometer. The morphologies of the samples were investigated by SEM using a Phenom-FEI apparatus. Raman spectra were measured using a micro-Raman spectrophotometer LabRam HR HORIBA Jobin Yvon equipped with a He-Ne (632.8 nm) laser source (20 mW) and a CCD detector. Surface area measurements were obtained by single point N_2 absorption using a Monosorb Quantachrome instrument. The HC electrode tapes were prepared by blending the HC active material obtained after ball milling (80 wt.%), Super-P carbon (10 wt.%, electronic conductor) and Kynar (10 wt.%, binder) in tetrahydrofuran (THF). The slurry was cast onto aluminium foils and, after solvent removal at room temperature, vacuum dried at 110 °C for 18 hours. Discs of 10/18 mm diameter were punched from the electrode tapes. The active material loading was about 3-4 mg cm^{-2}. Na/HC half-cells were assembled in glove box by using an El-Cell-REF cell assembly: an HC positive electrode, a sodium disk counter electrode and a borosilicate fiberglass separator 1.55 mm thick (El-Cell) were coupled and closed into the cell assembly. The separator was wetted by 100 microL of a non aqueous electrolyte (Solvionic) consisting of a 1 M solution of NaTFSI dissolved in PC with 3% by weight of FEC additive. A reference electrode consisting of a Na wire was inserted into the cell assembly orthogonal and in direct contact with the separator soaked with the electrolyte. The galvanostatic tests of the Na-half-cells were performed using a MTI battery tester at 30 °C (Memmert oven). The GC tests were performed in the 0.05-2.2 V electrode potential range, with various current rates. Capacities and current rates have been normalized to the mass of the active HC material: an approximate current rate conversion is proposed by assuming a theoretical capacity of 372 $mAhg^{-1}$ corresponding to a final 1:6 Na:C ratio in analogy to the electrochemical lithium insertion in the graphite lattice. EIS tests performed upon cycling (EIS, 10 mV AC amplitude in the 10^5-0.1 Hz frequency range) were carried out using a programmable Ivium Vertex EIS-Potentiostat/Galvanostat. EIS Spectrum Analyzer has been adopted to fit the EIS experimental data [31]. The spectra were recorded at the end of each full cycle in the charge state of the HC electrodes (de-sodiated state). TEM, Fast-Fourier Transform Infrared (FTIR) and X-ray photoelectron spectroscopies (XPS) were performed on pristine materials and on samples recovered after cycling in Na-cells. Materials have been recovered from the sodium cells and carefully washed: cells have been opened less than 30 minutes after the end of the electrochemical experiment and the electrodes washed three times in dried PC and THF, and finally dried at room temperature under vacuum. All these operations have been conducted in an Ar-filled glovebox. TEM experiments were carried out using a FEI Tecnai cryo-TEM in bright-field mode. FTIR experiments were performed by using a Bruker Alpha Instrument in attenuated total reflectance (ATR) mode using a Ge crystal. XPS experiments were performed with an in-house spectrometer (PHI 5500) using a monochromatized Al Kα radiation (hv = 1486.7 eV) as exciting source. All the photoionization regions were acquired using a take-off angle of 45° vs the sample surface normal and a constant pressure in the analyser chamber of 2×10^{-9} mbar during the all spectra detections. Before the XPS analyses, cells were disassembled in an Argon-filled glove box and washed with DMC and THF 4 times in order to remove any traces of electrolyte from the surfaces of the positive electrodes. After that, samples were transferred to the XPS analyser chamber using an air-tight transfer cup filled with Argon to avoid moisture, O_2 and CO_2 contaminations. Curve fitting of the experimental results was carried outed with Shirley functions for the backgrounds and with pseudo-Voigt functions, described by position, FWHM and Gaussian−Lorentzian ratio, for the elastic peaks. These parameters and their attributions to the chemical compounds are reported in table 1. The C 1s binding energy (BE) of the $–CF_2–CH_2–$ component (290.6-290.8 eV) was adopted as the internal standard reference for the BE scale among the different samples with an accuracy of ±0.1 eV. No degradation signals of the samples were observed during the XP spectra acquisitions.

Acknowledgements

JM would like to thank the University of St Andrews for her research stay. SB would like to thank the Italian Government for the funding through the FFARB scheme and Basilicata Innovazione project for the financial support through the specific program “Validazione dei risultati della Ricerca - Progetto di Convalida 2014-2015 - Prestazioni e analisi di fallimento di un dispositivo sodio-ione completo per accumulo reversibile di energia”. RY is grateful to the Swedish Research Council for Environment, Agricultural Sciences and Spatial Planning

(FORMAS)(project number 2016-01257) and STandUp for Energy for financial support.

Keywords: Sodium battery; hard carbon; Solid electrolyte interphase; SEI.

[1] C. Delmas, *Adv. Energy Mater.* **2018**, *8*, 17.
[2] S. Roberts, E. Kendrick, *Nanotechnol. Sci. Appl.* **2018**, *11*, 23–33.
[3] N. Ortiz-Vitoriano, N. E. Drewett, E. Gonzalo, T. Rojo, *Energy Environ. Sci.* **2017**, *10*, 1051–1074.
[4] C. Wu, S.-X. Dou, Y. Yu, *Small* **2018**, *14*, 22.
[5] E. Irisarri, A. Ponrouch, M. R. Palacin, *J. Electrochem. Soc.* **2015**, *162*, A2476–A2482.
[6] R. Mogensen, D. Brandell, R. Younesi, *ACS Energy Lett.* **2016**, *1*, 1173–
[7] M. Á. Muñoz-Márquez, D. Saurel, J. L. Gómez-Cámer, M. Casas-Cabanas, E. Castillo-Martínez, T. Rojo, *Adv. Energy Mater.* **2017**, *7*, 20.
[8] G. Hasegawa, K. Kanamori, N. Kannari, J. Ozaki, K. Nakanishi, T. Abe, *ChemElectroChem* **2015**, *2*, 1917–1920.
[9] X. Dou, I. Hasa, M. Hekmatfar, T. Diemant, R. J. Behm, D. Buchholz, S. Passerini, *ChemSusChem* **2017**, *10*, 2668–2676.
[10] W. Xing, J. S. Xue, J. R. Dahn, *J. Electrochem. Soc.* **1996**, *143*, 3046.
[11] J. R. Dahn, W. Xing, Y. Gao, *Carbon N. Y.* **1997**, *35*, 825–830.
[12] C. Bommier, W. Luo, W.-Y. Gao, A. Greaney, S. Ma, X. Ji, *Carbon N. Y.* **2014**, *76*, 165–174.
[13] J. Song, B. Xiao, Y. Lin, K. Xu, X. Li, *Adv. Energy Mater.* **2018**, *8*, 17.
[14] P. Verma, P. Maire, P. Novák, *Electrochim. Acta* **2010**, *55*, 6332–6341.
[15] M. Holzapfel, A. Würsig, W. Scheifele, J. Vetter, P. Novák, *J. Power Sources* **2007**, *174*, 1156–1160.
[16] D. Aurbach, B. Markovsky, G. Salitra, E. Markevich, Y. Talyossef, M. Koltypin, L. Nazar, B. Ellis, D. Kovacheva, *J. Power Sources* **2007**, *165*, 491–499.
[17] D. Aurbach, M. D. Levi, E. Levi, H. Teller, B. Markovsky, G. Salitra, U. Heider, L. Heider, *J. Electrochem. Soc.* **1998**, *145*, 3024–3034.
[18] S. Komaba, W. Murata, T. Ishikawa, N. Yabuuchi, T. Ozeki, T. Nakayama, A. Ogata, K. Gotoh, K. Fujiwara, *Adv. Funct. Mater.* **2011**, *21*, 3859–3867.
[19] F. A. Soto, P. Yan, M. H. Engelhard, A. Marzouk, C. Wang, G. Xu, Z. Chen, K. Amine, J. Liu, V. L. Sprenkle, et al., *Adv. Mater.* **2017**, *29*, 1606860.
[20] D. A. Stevens, J. R. Dahn, *J. Electrochem. Soc.* **2000**, *147*, 1271.
[21] S. Shi, P.Lu, Z.Liu, Y.Qi, L.G. Hector Jr., H. Li, S.J. Harris. *J. Am. Chem. Soc*. **2012**, *134*, 15476-15487.
[22] S. Shi, Y. Qi, H. Li, L.G. Hector. . *Phys. Chem. C* **2013**, *117*, 8579-8593.
[23] A. Wang, S. Kadam, H.Li, S. Shi, Y. Qi. *Npj Comp. Mater.* **2018**, *4*, 15.
[24] S. Shi, J. Gao, Y. Liu, Y. Zhao, Q. Wu, W. Ju, C. Ouyang, R. Xiao. *Chin. Phys. B* **2016**, *25*, 018212.
[25] X. Xia, W. M. Lamanna, J. R. Dahn, *J. Electrochem. Soc.* **2013**, *160*, A607–A609.
[26] A. Ponrouch, A. R. Goñi, M. R. Palacín, *Electrochem. commun.* **2013**, *27*, 85–88.
[27] M. Dahbi, T. Nakano, N. Yabuuchi, S. Fujimura, K. Chihara, K. Kubota, J.-Y. Son, Y.-T. Cui, H. Oji, S. Komaba, *ChemElectroChem* **2016**, *3*, 1856–1867.
[28] J. Wen, Y. Yu, C. Chen, *Mater. Express* **2012**, *2*, 197–212.
[29] C. Arbizzani, G. Gabrielli, M. Mastragostino, *J. Power Sources* **2011**, *196*, 4801–4805.
[30] R. Younesi, G. M. Veith, P. Johansson, K. Edström, T. Vegge, *Energy Environ. Sci.* **2015**, *8*, 1905–1922.
[31] Bondarenko A. S., Ragoisha G. A., in *Prog. Chemom. Res.* (Ed.: A.L. Pomerantsev), Nova Science Publishers, New York (USA), **2005**, pp. 89–102.
[32] F. Bonino, S. Brutti, M. Piana, S. Natale, B. Scrosati, L. Gherghel, K. Müllen, *Electrochim. Acta* **2006**, *51*, 3407–3412.
[33] F. Bonino, S. Brutti, M. Piana, B. Scrosati, L. Brambilla, G. Fustella, C. Castiglioni, G. Zerbi, D. Zane, T. Renouard, et al., *J. Electrochem. Soc.* **2005**, *152*, A2023–A2029.
[34] F. Bonino, S. Brutti, P. Reale, B. Scrosati, L. Gherghel, J. Wu, K. Müllen, *Adv. Mater.* **2005**, *17*, 743–746.
[35] A. C. Ferrari, *Solid State Commun.* **2007**, *143*, 47–57.
[36] S. J. R. Prabakar, J. Jeong, M. Pyo, *Electrochim. Acta* **2015**, *161*, 23–31.
[37] K. Hong, L. Qie, R. Zeng, Z. Yi, W. Zhang, D. Wang, W. Yin, C. Wu, Q. Fan, W. Zhang, et al., *J. Mater. Chem. A* **2014**, *2*, 12733.
[38] P. Lu, C. Li, E. W. Schneider, S. J. Harris, *J. Phys. Chem. C* **2013**, 131219170849009.
[39] J. Højberg, B. D. McCloskey, J. Hjelm, T. Vegge, K. Johansen, P. Norby, A. C. Luntz, *ACS Appl. Mater. Interfaces* **2015**, *7*, 4039–4047.
[40] E. Peled, D. Golodnitsky, G. Ardel, *J. Electrochem. Soc.* **1997**, *144*.
[41] K. E. Aifantis, S. Brutti, S. A. Hackney, T. Sarakonsri, B. Scrosati, *Electrochim. Acta* **2010**, *55*, 5071–5076.
[42] S. Vahur, A. Teearu, P. Peets, L. Joosu, I. Leito, *Anal. Bioanal. Chem.* **2016**, *408*, 3373–3379.
[43] Z. Guan, H. Liu, B. Xu, X. Hao, Z. Wang, L. Chen, *J. Mater. Chem. A* **2015**, *3*, 7849–7854.
[44] Y. Pan, Y. Zhang, B. S. Parimalam, C. C. Nguyen, G. Wang, B. L. Lucht, *J. Electroanal. Chem.* **2017**, *799*, 181–186.
[45] P. M. T. M. van Attekum, G. K. Wertheim, *Phys. Rev. Lett.* **1979**, *43*, 1896–1898.
[46] R. I. . Blyth, H. Buqa, F. . Netzer, M. . Ramsey, J. . Besenhard, P. Golob, M. Winter, *Appl. Surf. Sci.* **2000**, *167*, 99–106.
[47] F. Sette, G. K. Wertheim, Y. Ma, G. Meigs, S. Modesti, C. T. Chen, *Phys. Rev. B* **1990**, *41*, 9766–9770.
[48] G. Speranza, L. Minati, *Surf. Sci.* **2006**, *600*, 4438–4444.
[49] M. Carboni, S. Brutti, A. G. Marrani, *ACS Appl. Mater. Interfaces,* **2015**, *7*, 21751–21762.
[50] F. Bournel, C. Laffon, P. Parent, G. Tourillon, *Surf. Sci.* **1996**, *350*, 60–78.
[51] D. (David) Briggs, M. P. Seah, *Practical Surface Analysis*, Wiley, **1990**.
[52] R. Mogensen, J. Maibach, A.J. Naylor, R. Younesi, *Dalt. Trans.* **2018**, *47*, 10752–10758..
[53] E. Björklund, D. Brandell, M. Hahlin, K. Edström, R. Younesi, *J. Electrochem. Soc.* **2017**, *164*, A3054–A3059.
[54] R. Younesi, F. Bardé, *Sci. Rep.* **2017**, *7*, 15925..
[55] D. Giacco, M. Carboni, S. Brutti, A. G. Marrani, *ACS Appl. Mater. Interfaces* **2017**, *9*, 31710–31720.
[56] B. Philippe, M. Hahlin, K. Edström, T. Gustafsson, H. Siegbahn, H. Rensmo, *J. Electrochem. Soc.* **2016**, *163*, A178–A191.
[57] K. Kanamura, S. Shiraichi, H. Takezawa, Z.-I. Takehara, *Chem. Mater.* **1997**, *9*, 1797–1804.
[58] F. Vautard, S. Ozcan, H. Meyer, *Compos. Part A Appl. Sci. Manuf.* **2012**, *43*, 1120–1133.
[59] H.-K. Jeong, Y.-P. Lee, R. J. W. E. Lahaye, M.-H. Park, K.-H. An, I. J. Kim, C.-W. Yang, C.-Y. Park, R. S. Ruoff, Y. H. Lee, *J. Am. Chem. Soc.* **2008**, *130*, 1362–1366.
[60] M. Carboni, A. G. A. G. Marrani, R. Spezia, S. Brutti, *J. Electrochem. Soc.* **2018**, *165*, 1–9.
[61] H. Estrade-Szwarckopf, *Carbon N. Y.* **2004**, *42*, 1713–1721.
[62] G. Beamson, D. Briggs, *High Resolution XPS of Organic Polymers, the Scienta ESCA300 Database*, Wiley, Chichester, **1992**.
[63] T. Jaumann, J. Balach, M. Klose, S. Oswald, J. Eckert, L. Giebeler, *J. Electrochem. Soc.* **2016**, *163*, A557–A564.
[64] N.-S. Choi, Y. Lee, S.-S. Kim, S.-C. Shin, Y.-M. Kang. *J. Power Sources* **2010**, *195*, 2368-2371
[65] A. Shchukarev, D. Korolkov, *Open Chem.* **2004**, *2*, 347–362.
[66] "NIST X-ray Photoelectron Spectroscopy Database," can be found under http://srdata.nist.gov/xps/, **2012**.